



## **EVALUATION OF FRANCIS TURBINE AERATION AS A MEASURE TO ATTENUATE PRESSURE PULSATIONS**

**João Maria Marra**

marra@itaipu.gov.br

Itaipu Binacional

6731 Av. Tancredo Neves, 85866-900, Paraná, Foz do Iguaçu, Brazil

**Liliana Gramani**

l.gramani@gmail.com

Universidade Federal do Paraná

210 Av. Cel Francisco Heráclito dos Santos, 80210-170, Paraná, Curitiba, Brazil

**Luan Malikoski Vieira**

luan\_malikoski@hotmail.com

Universidade Estadual do Oeste do Paraná - UNIOESTE

Centro de Estudos Avançados em Segurança de Barragens- CEASB –FPTI-BR

6731 Av. Tancredo Neves, 85867-900, Paraná, Foz do Iguaçu, Brasil

**Eloy Kaviski**

eloy.dhs@ufpr.br

Universidade Federal do Paraná

Jardim das Américas, 81530-000, Paraná, Curitiba, Brazil

**Abstract.** *When operating in off-design conditions, Francis Hydraulic Turbines features flow phenomena related with low-frequency pressure pulsations. Those pulsations mechanisms can lead the system to resonance or instabilities. In this situation, high-pressure pulsations can cause structural or mechanical components failure, wear by cavitation, besides reducing energy generation quality. Inserting air into the draft tube is one of the most common measure to mitigate pressure pulsations. In this panorama, the present work aim to apply a one-dimensional distributed parameter mathematical model of the hydraulic circuit of a*

Francis turbine in order to predict full load instability. The Vortex hydroacoustic parameters are computed by CFD simulations. In order to verify the model, and evaluate aeration effectiveness, a design of a mechanical device that can control the axial atmospheric aeration valve to enable tests in a turbine prototype is developed. Further, field tests shows that a discharge of air of 1.3% of the rated discharge can reduce pressure pulsations by 90% in a specific full load operating point. Also, in this case study applied to ITAIPU turbines, the mathematical modelling result has successfully predict full load instability observed in field test under variation of aeration level.

**Keywords:** Francis turbine, Aeration, Hydraulic Instability, CFD.

## 1 INTRODUCTION

There is global trend to operate Francis hydraulic turbines in a broad range. Due to its flexibility, those turbines have the role to stabilize the electrical grid making off-design operations quite common.

Non- adjustable blades Francis turbines features instabilities in off-design conditions with critical operation zones where low frequency pressure pulsations are present in the draft tube. Such pulsations are generally results of vortex, with low - pressure region, formed at runner exit (Lipej et. al., 2009; Pejovic, 2002; Müller, 2014). Those vortexes are distinguished between full load vortex rope and full load vortex core as observed in Fig. 1.

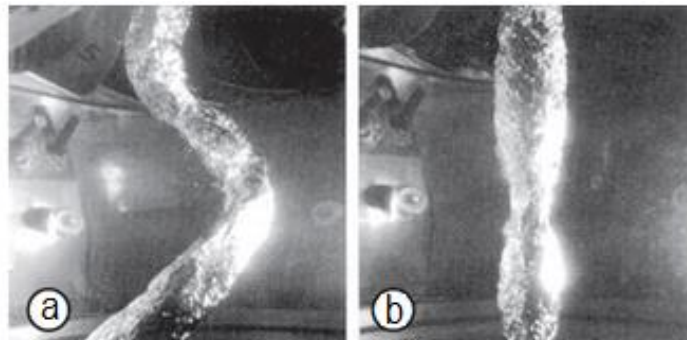


Figure 1 – (a) Part load vortex rope; (b) Full load vortex core (Adapted from Nicolet, 2007)

At part load ( $Q < Q_n$ ) the vortex, in Figure 1 (a), has a helical shape, with a precession motion in the same direction as the tangential component of the absolute flow velocity  $C_u$  or runner rotation at blade outlet  $U_1$ , in Figure 2 (a). At full load, ( $Q > Q_n$ ) the vortex, in Figure 1 (b), has an axisymmetric shape with its core rotating in same direction as the tangential component of the absolute flow velocity  $C_u$  or opposite direction as runner rotation.

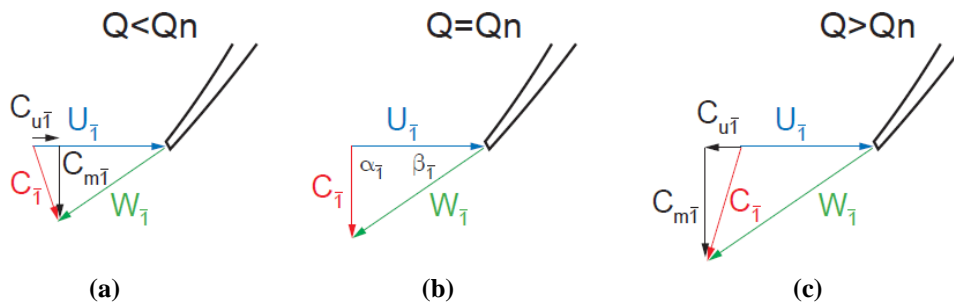


Figure 2 - Velocity triangles – (a) Part load; (b) Design; (c) Full load (Adapted from Nicolet, 2007)

The static pressure conversion into dynamic pressure, due to the flow tangential momentum at runner outlet, enables biphasic composition in the vortex core by means of cavitation phenomena (Landry, 2015; Dörfler et. al 2013).

At part load, the vortex precession frequency ( $\sim 0.27f_n$ ) may match the draft tube natural frequency, given by Eq.(1), leading the system to resonance. At full load conditions, high-pressure fluctuations may arise from the system instability or auto - excitation.

$$f_0 = \frac{1}{2\pi} \sqrt{\frac{gA}{dxC_{eq}}} \quad (1)$$

From Eq. (1),  $C_{eq}$  is the draft tube equivalent compressibility given by Eq. (2),  $g$  the gravity constant,  $A$  the draft tube cross section area,  $dx$  the draft tube characteristic length and  $a_{eq}$  the draft tube equivalent wave speed.

$$C_{eq} = \frac{gAdx}{a_{eq}^2} \quad (2)$$

Inserting air into the draft tube flow, under the runner, is the most common measure to reduce pressure pulsations and cavitation. This technic can alter the draft tube hydroacoustic characteristics (Nicolet, 2007; Alligné, 2011; Dörfler et. al, 2013) changing excitation amplitudes and frequencies. Also, it reduce draft tube natural frequencies by lowering its equivalent wave speed ( $a_{eq}$ ) and increasing its equivalent compressibility ( $C_{eq}$ ) which may eliminate tune with excitation sources (Pejovic, 1986; Lecher Apud Dörfler et. al, 2013; Nakanishi Apud Dörfler et. al, 2013).

The vortex core, at full load conditions, is mathematically represented by two parameters, named as Cavitation Compliance ( $C$ ) and Mass Flow Gain Factor ( $\chi$ ). The first one is related with the vortex core compressibility and natural frequency of pulsation whereas the second one is associated with the system damping and is interpreted as an instability source (Chen et. al., 2008, Alligné, 2011, Flemming et. al., 2009).

## 2 PROTOTYPE CHARACTERISTICS

The studies and field tests are performed in one of the 20 ITAIPU Hydroelectric Powerplant generating units (Unit 9), installed at Paraná River in Foz do Iguazu – Brazil. Each unit features a Francis turbine with 715MW of rated power, 113 m of rated head, design discharge ( $Q_{BEP}$ ) of 570 m<sup>3</sup>/s, 92.3 RPM (1.53Hz) of runner rotation and 231.2 RPM of specific speed.

### 2.1 Prototype aeration system

The prototype has one axial aeration system, seen in Figure 3 (a), which inserts air into the draft tube, just under the runner. A valve, Figure 3 (b), which rotates with the generator shaft, controls the airflow.

This valve is an auto-controlled one, as a mass-spring-damper system, and opens when the pressure difference between its obturator upstream (atmospheric pressure) and downstream (draft tube pressure or vortex core pressure) is enough to overcome its spring pre-load. It has a maximum opening of 150 mm, besides acceptance field tests stated that its maximum opening is around 45 mm when free to oscillate and the unit is generating 700MW

(full load condition). This application has the goal of attenuate pressure pulsations in full load conditions, which has a frequency of  $\sim 1.4\text{Hz}$  in this case (ITAIPU, 2015).

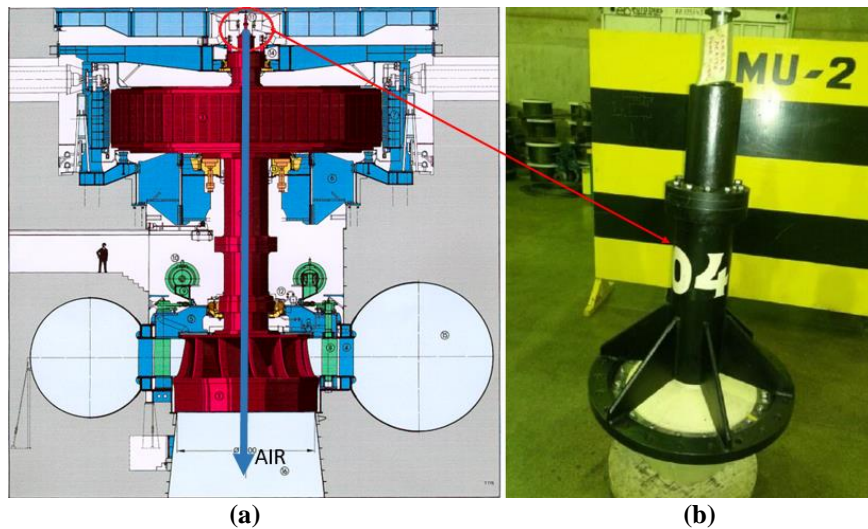


Figure 3 - ITAIPU's turbines aeration system – (a) Air path; (b) Aeration Valve (ITAIPU, 2015).

## 2.2 Aeration system adaptation

In order to evaluate the aeration effect over the dynamical response of the system, a mechanical device to control the aeration valve, seen in Figure 4, was designed.

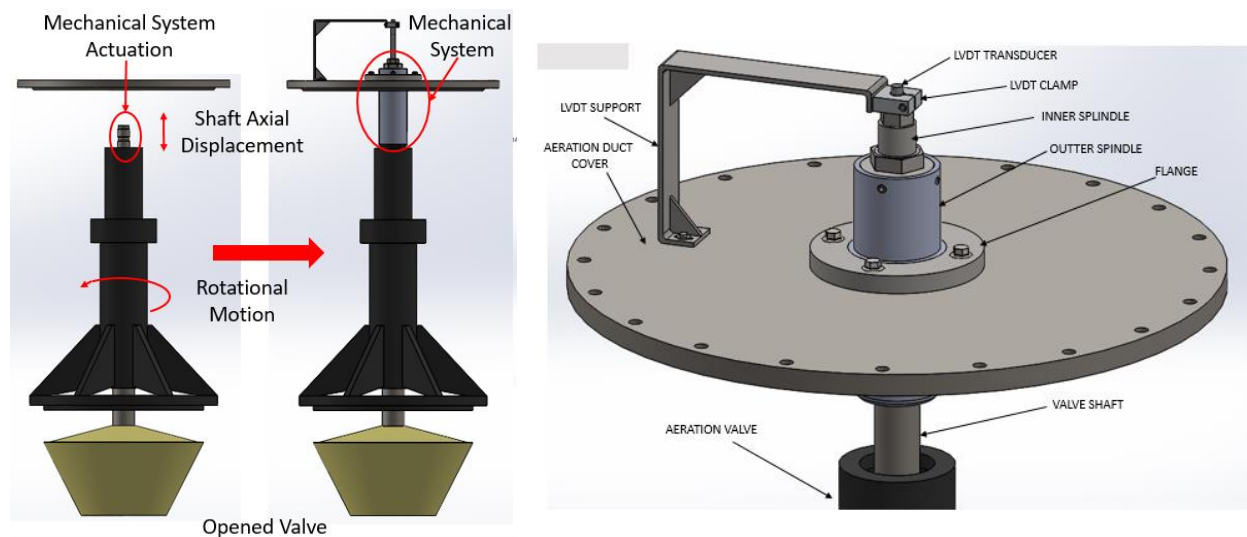


Figure 4 – Mechanical system of aeration valve control

This device acts in the valve shaft tip controlling its axial motion and has the capability of lock the valve in any desired position or limit its displacement inside any pre-determined range by manual action during generating unit operation. This system also features a LVDT transducer to track the valve shaft displacement and a piezometric pressure transducer to measure indirectly the airflow in the aeration duct. Figure 5 shows the device assembly in generation Unit 9 where tests were performed.



Figure 5 – Mechanical device assembly at U9 (ITAIPU, 2015)

### 3 PROTOTYPE FIELD TESTS

The hydraulic system dynamic response evaluation is based on pressure signals from probes located at Spiral Case inlet (SC1) and Draft Tube (DT1). The data sampled at 600Hz in 40s interval is processed by *FFT*, with a *hamming* window and a *butterworth* filter of 14<sup>th</sup> order and cut-off frequency of 21Hz.

#### 3.1 Aeration effect over hydraulic system dynamic response

The first investigations were performed under a net Head of 116m ( $H_{\text{upstream}}= 217\text{m}$  e  $H_{\text{downstream}}= 101\text{m}$ ). In this case, the active power output was changed from 450MW (part load) to 740MW (full load) as described in Table 1.

Table 1 – Test operating points

Test Point	$\bar{P}_{At}$ [MW]	$\bar{Q}$ [m <sup>3</sup> /s]	$\bar{Q}/Q_{\text{BEP}}$ [-]	Wicked gate opening [%]
1	455	411	0.72	48.80
2	503	450	0.79	53.20
3	542	479	0.84	56.80
4	590	520	0.91	61.90
5	668	597	1.05	74.40
6	683	621	1.09	78.90
7	743	703	1.23	96.25

For each test point, pressure signals were measured for both conditions: free aeration valve and closed aeration valve. For this analysis, the oscillating part of the pressure signal was taken by subtracting the mean value from the unsteady pressure signal using Eq. (3).

$$P(t) = \bar{P} + P' \quad (3)$$

In Figure 6, cascades diagrams compare pressure fluctuations amplitudes, made non-dimensional by the turbine specific pressure, and frequency for both valve-opening cases at Spiral Case (SC1) and Draft Tube (DT1) for each operating test point.

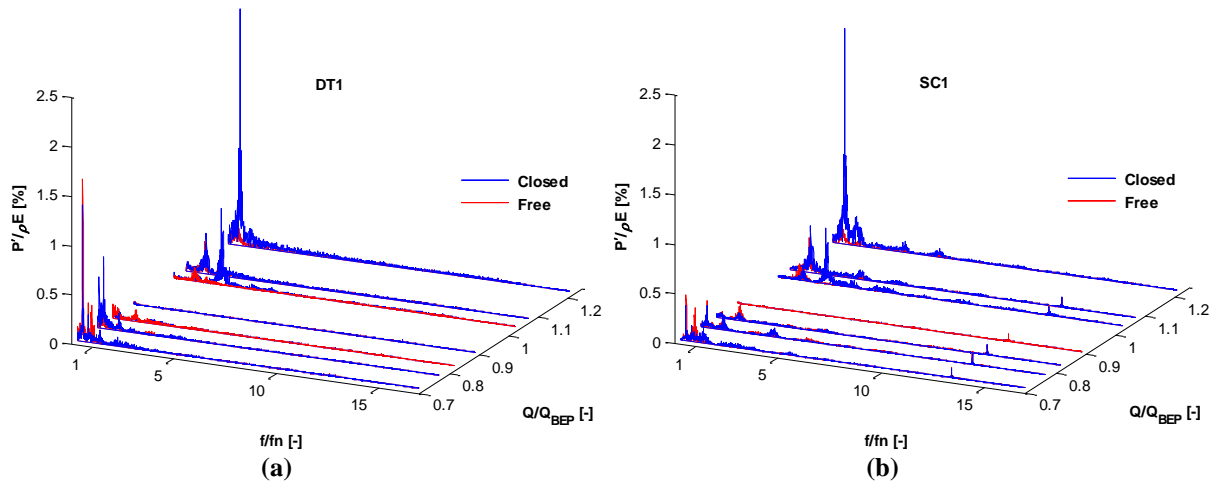


Figure 6 – Pressure oscillations comparison – (a) DT1; (b) SC1

Figure 7 compare the dominant frequency in SC1 and DT1 signals through the test range for both valve opening case.

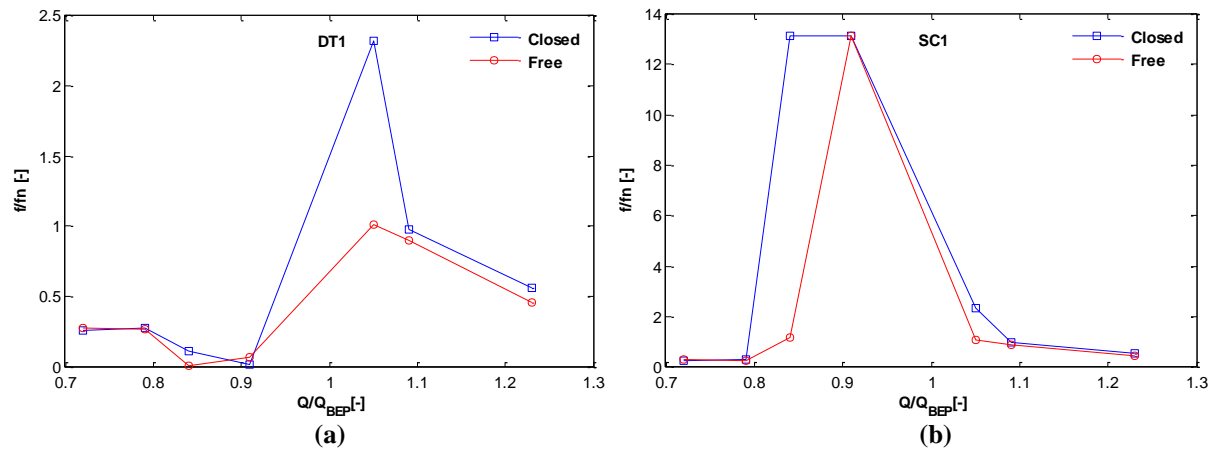


Figure 7 – Dominant frequency comparison – (a) DT1; (b) SC1

For the test points 3 ( $Q/Q_{BEP} = 0.84$ ) and 4 ( $Q/Q_{BEP} = 0.91$ ), in Figure 6 (b) and Figure 7 (b), the pressure signal features a frequency of  $13 \cdot f_n$  which is the prototype blade passing frequency. Table 2 shows the change in the dominant frequency upon aeration.

Table 2 – Change in dominant frequency

Test	$Q/Q_{BEP}$	$f/f_n[-]$ - Closed		$f/f_n[-]$ - Free		$\Delta f$ [%]	
		DT1	SC1	DT1	SC1	DT1	SC1
1	0.72	0.26	0.26	0.27	0.27	4.7	4.7
2	0.79	0.28	0.28	0.27	0.27	-4.3	-4.3
3	0.84	1.16	1.16	1.16	1.16	0.0	0.0
4	0.91	-	-	-	-	-	-
5	1.05	2.31	2.31	1.01	1.05	-56.2	-54.6
6	1.09	0.98	0.98	0.90	0.90	-8.1	-8.1
7	1.23	0.56	0.56	0.46	0.46	-18.5	-18.5

For both pressure signals (SC1 and DT1), at full load conditions (Test points 5, 6 and 7), the dominant frequency is reduced upon aeration. For part load conditions, the dominant frequency ( $\sim 0.27 \cdot f_n$ , vortex precession frequency or *Reighnaz* frequency) do not change with aeration, result that is also found by Qian (2006).

With respect to pressure pulsations amplitudes, aeration presented to be beneficial for full load conditions (Tests 5, 6 and 7) reducing those amplitudes up to 90%. In contrast, for part load conditions, pressure pulsations were increased upon aeration, however the amplitudes difference involved are small, as shown in Figure 8. Thus, there is no clear tendency for the aeration effect over pressure pulsations amplitude in part load operation conditions.

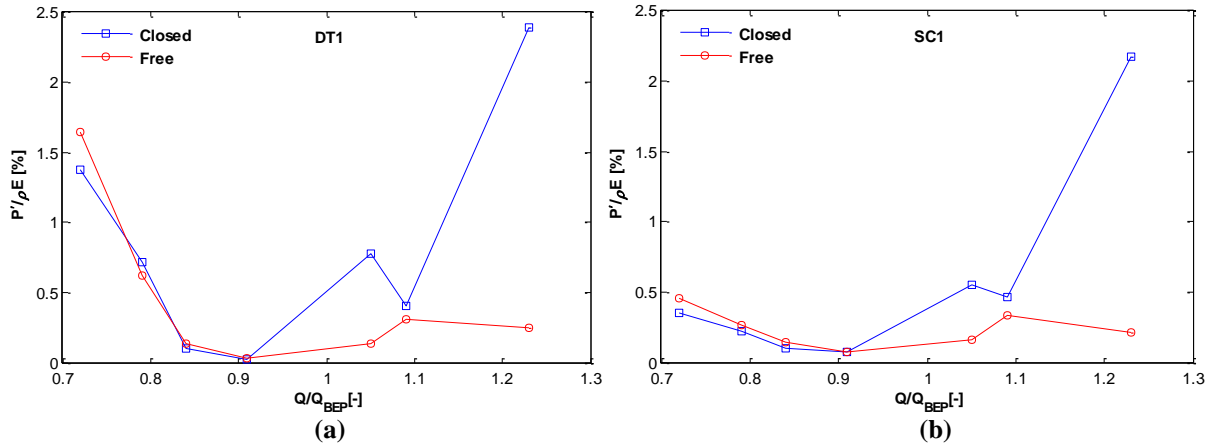


Figure 8 – Pressure pulsations amplitude comparison – (a) DT1; (b) SC1

Table 3 summarizes the results for the change in pressure pulsations ( $\Delta P'$ ) upon aeration, in both hydraulic system positions (SC1 and DT1).

Table 3 – Change in pressure fluctuation

Test	Q/Q <sub>BEP</sub>	P'/ρE [%]-Closed		P'/ρE [%] - Free		ΔP' [%]	
		DT1	SC1	DT1	SC1	DT1	SC1
1	0.72	1.38	0.35	1.65	0.46	19.8	30.5
2	0.79	0.72	0.23	0.62	0.27	-13.1	18.6
3	0.84	0.10	0.10	0.14	0.15	31.1	49.2
4	0.91	0.03	0.08	0.03	0.08	14.8	0.8
5	1.05	0.78	0.56	0.14	0.17	-82.4	-69.6
6	1.09	0.41	0.47	0.32	0.34	-23.1	-27.3
7	1.23	2.39	2.17	0.25	0.22	-89.6	-90.0

Power output pulsation was increased upon aeration in part load conditions ( $Q/Q_{BEP} < 1$ ), however, a significant change was found for the Test 7 (full load), where power oscillation were reduced by 57%, as shown in Figure 9.

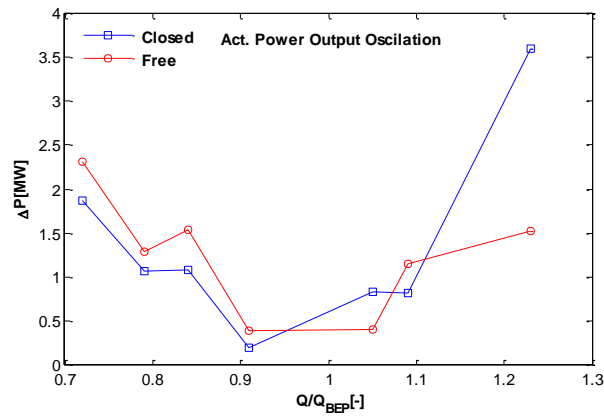


Figure 9 – Change in power output oscillation

### 3.2 Variation of the opening limit of the aeration valve

In this section, aeration effect is evaluated for the operating point 7 ( $Q/Q_{BEP} = 1.23$ ) as the opening limit of the aeration valve is changed. Even though this valve has its maximum opening limit of 150 mm when free to oscillate, for this operating condition, the maximum opening was found to be around 30 mm during late tests. This way, the mechanical device was configured in order to limit the valve oscillation inside successive pre-defined ranges of 8%, 21% and 36% of that measured maximum value, as shown in Table 4.

Table 4 – Valve opening limit for each test

Test	Max Limit [mm]	Max Limit /Max [%]
1	Closed	0
2	2.4	8
3	6.5	21
4	11.0	36
5	30.0 (Free)	100

Figure 10 shows frequency response of pressure signals SC1 and DT1 for those five test cases.

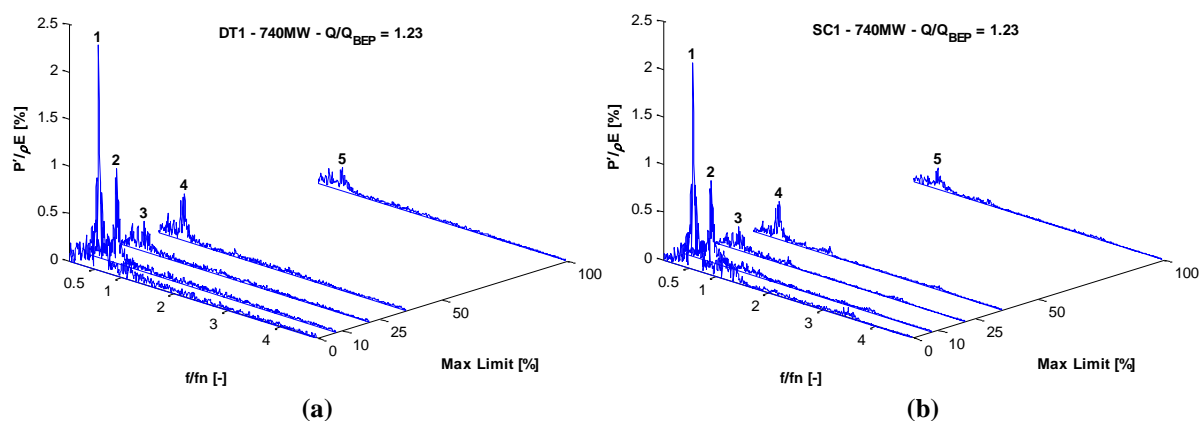


Figure 10 – Pressure oscillation – (a) DT1; (b) SC1

Results for dominant frequency and oscillation amplitude of Pressure, Power output (P) and discharge (Q) for each opening valve limit is shown in Table 5.

**Table 5 – Pressure, power and discharge oscillation**

Max Limit [%]	f/fn [-]		P'/ρE		f/fn		P[W]	Q [m <sup>3</sup> /s]
	DT1	SC1	DT1	SC1	P	Q	ΔP	ΔQ
0	0.56	0.56	2.39	2.17	0.56	0.05	3.59	4.18
8	0.53	0.53	1.00	0.86	0.53	0.18	1.62	3.42
21	0.43	0.43	0.32	0.25	0.21	0.27	0.95	4.30
36	0.49	0.49	0.50	0.40	0.04	0.21	1.72	3.93
100	0.46	0.46	0.25	0.22	0.05	0.14	1.53	3.46

Figure 11 (a) shows the evolution of the dominant frequency for pressure signals (DT1 and (SC1), Power (P) and Discharge (Q) as the valve opening limit is increased.

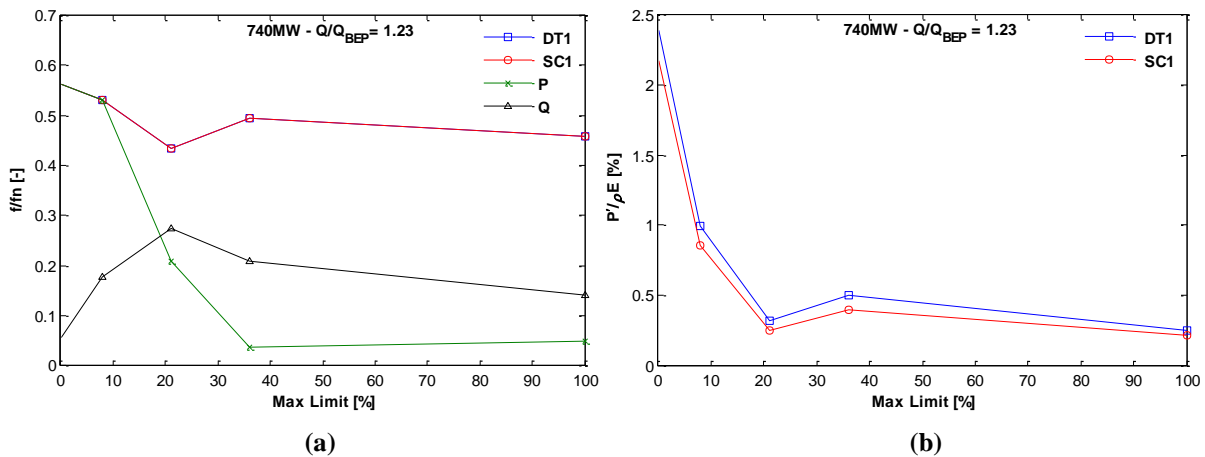


**Figure 11 – (a) Dominant Frequency; (b) Pressure oscillation amplitude**

It can be observed that for the whole range of valve opening limit, pressure dominant frequency at DT1 and SC1 probes are coincident and are reduced up to 23% in an almost linear relation with the aeration valve-opening limit. In addition, the Power (P) output dominant frequency is reduced and its tune with pressure pulsation frequency is extinguished after 36% of valve maximum opening limit.

Figure 11 (b) shows the evolution of oscillations amplitude for pressure signals (DT1 and SC1) as the valve opening limit is increased. Pressure oscillation amplitude at draft tube (DT1) was always a little greater than those amplitudes at spiral case (SC1) in all range. For both signals, amplitudes were vertiginously decreased in the interval between 0% opening to 21% opening, as shown in Figure 11 (b). After this interval, pressure amplitudes tend to be constant until the free valve oscillation condition.

Mean air discharge for each test case was measured and is made non-dimensional by the mean water rated discharge as shown in Table 6. Those results for air discharge explain the virtually invariant dynamical response of the system in terms of frequency and amplitude of pressure pulsations after 21% of max limit of valve opening, once the air discharge beyond

this point is no longer changed. The reduction in dominant frequency as air discharge increases is clear, fact corroborated by theory and observed by Pejovic (1986).

Table 6 – Air discharge

Test	Opening	Air Discharge
	Max Limit [%]	$Q_{air}/\bar{Q}$ [%]
1	0	0.0
2	8	1.0
3	21	1.3
4	36	1.3
5	100	1.2

Figure 12 shows the aeration effect in time domain, where the pressure oscillation amplitude is clearly reduced when air is admitted into draft tube (free valve condition).

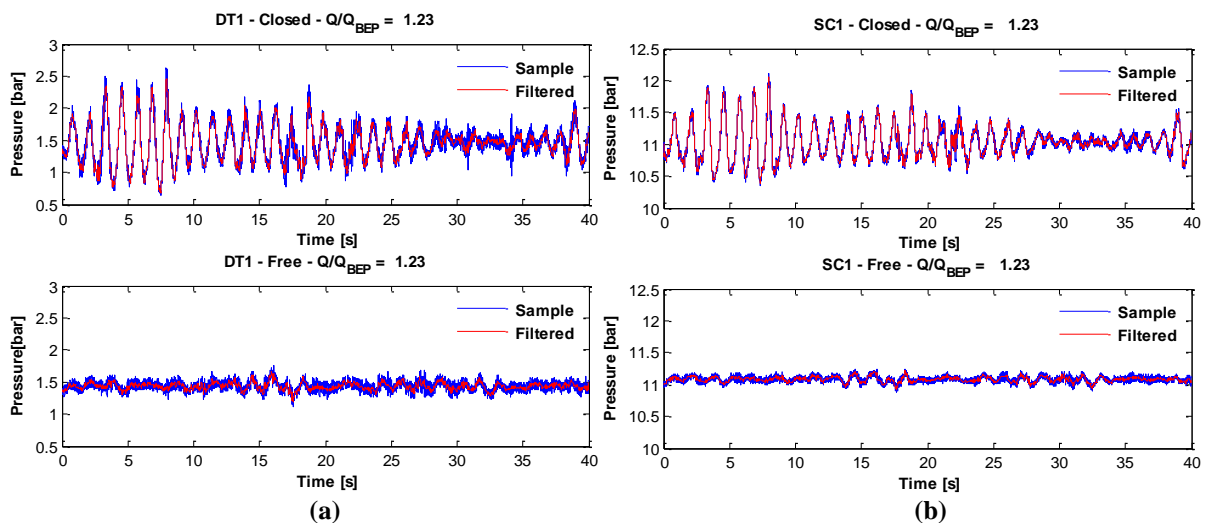


Figure 12 - Time domain response - (a) DT1; (b) SC1

#### 4 MATHEMATICAL MODEL

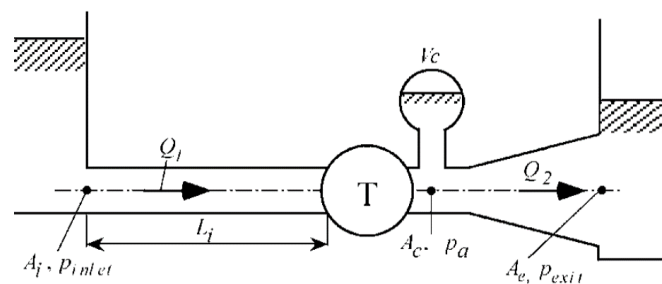


Figure 13 – Simplified hydraulic system (Chen et al, 2008)

Considering an ideal one-dimensional hydraulic system, as the one in Figure 13, composed of a penstock of length  $L_i$  and cross-section area  $A_i$ , a draft tube with an equivalent

length  $L_e$  and outlet cross-section area  $A_e$ , continuity equation relating the vortex volume  $V_c$ , upstream discharge  $Q_1$  and downstream discharge  $Q_2$  can be written as follows.

$$Q_2 - Q_1 = \frac{dV_c}{dt} \quad (4)$$

Momentum conservation law can be applied to the vortex volume ( $V_c$ ) upstream and downstream sections of the hydraulic system, which result in Eq.(5) and Eq. (6).

$$p_i = p_a + \rho \frac{L_i}{A_i} \frac{dQ_1}{dt} + \rho \frac{\zeta_T}{2A_i^2} Q_1^2 \quad (5)$$

$$p_a = p_e + \rho \frac{L_e}{A_e} \frac{dQ_2}{dt} + \rho \frac{\zeta_2 - \delta}{2A_e^2} Q_2^2 \quad (6)$$

Where  $p_i$ ,  $p_a$  and  $p_e$  are pressure at penstock inlet, pressure at runner outlet and pressure at draft tube outlet respectively. Turbine and adduction losses are attributed to  $\zeta_T$ , whereas draft tube losses are accounted by  $\zeta_2$ . Draft tube diffusion factor  $\delta$  is given by  $\delta = (A_e/A_c)^2 - I$ , where  $A_c$  is the runner outlet area. By considering the presence of a cavitating vortex and its volume variation depending upon its core pressure  $p_c$  and upstream discharge  $Q_2$ , mass conservation law is applied as follows.

$$Q_2 - Q_1 = \frac{dV_c}{dt} = \frac{\partial V_c}{\partial p_c} \frac{dp_c}{dt} + \frac{\partial V_c}{\partial Q} \frac{dQ}{dt} = -C \frac{dp_c}{dt} - \chi \frac{dQ_2}{dt} \quad (7)$$

Where  $C$  is the Cavitation Compliance, or the vortex compressibility, and  $\chi$  the Mass Flow Gain Factor, which is considered as source of instabilities in the system.

The pressure drop at vortex core is related with the flow tangential momentum by Eq. (8). Same approach is used by Chen et. al (2008). Where  $C_\theta$ , stands for tangential velocity at runner blade outlet. Swirl pressure coefficient is given by  $\alpha$ .

$$p_c = p_a - \rho \alpha C_{\theta 2}^2 \quad (8)$$

From the velocity triangle at runner blade outlet, Eq. (10) can be written. Where  $U_2$ ,  $\beta_2$  and  $S$  are the runner exit peripheral speed, blade exit angle and runner exit area respectively.

$$C_\theta = C_{m2} \cot \beta_2 - U_2 = \frac{Q_1}{S} \cot \beta_2 - U_2 \quad (9)$$

After inserting equations (6) and (9) into Eq.(8), the result is derivate in relation of time and inserted into the continuity equation (7) which leads to equation (10).

$$Q_2 - Q_1 = -\rho C \frac{L_e}{A_e} \frac{d^2 Q_2}{dt^2} + \rho C \frac{\delta - \zeta_2}{A_e^2} Q_2 \frac{dQ_2}{dt} + 2\rho C \alpha \frac{\cot \beta_2}{S} \left( \frac{\cot \beta_2}{S} Q_1 - U_2 \right) \frac{dQ_1}{dt} - \chi \frac{dQ_2}{dt} \quad (10)$$

Putting Eq.(5) into Eq.(6) we obtain.

$$p_i = p_e + \rho \frac{L_e}{A_e} \frac{dQ_2}{dt} + \rho \frac{\zeta_2 - \delta}{2A_e^2} Q_2^2 + \rho \frac{L_i}{A_i} \frac{dQ_1}{dt} + \rho \frac{\zeta_T}{2A_i^2} Q_1^2 \quad (11)$$

Equations (10) and (11) are the dynamical system governing equations that after being linearized results in equations (12) and (13).

$$\tilde{Q}_2 - \tilde{Q}_1 = -\rho C \frac{L_e}{A_e} \frac{d^2 \tilde{Q}_2}{dt^2} + \rho C \frac{\delta - \zeta_2}{A_e^2} \tilde{Q} \frac{d\tilde{Q}_2}{dt} + 2\rho C \alpha \frac{\cot \beta_2}{S} \left( \frac{\cot \beta_2}{S} \tilde{Q} - U_2 \right) \frac{d\tilde{Q}_1}{dt} - \chi \frac{d\tilde{Q}_2}{dt} \quad (12)$$

$$0 = \rho \frac{L_e}{A_e} \frac{d\tilde{Q}_2}{dt} + \rho \frac{\zeta_2 - \delta}{A_e^2} \tilde{Q}_2 + \rho \frac{L_i}{A_i} \frac{d\tilde{Q}_1}{dt} + \rho \frac{\zeta_T}{A_i^2} \tilde{Q}_1 \quad (13)$$

For stability analysis, complex exponentials are applied, thus, we assume  $\tilde{Q}_1 = \tilde{Q}_{1,0}e^{-j\omega t}$  and  $\tilde{Q}_2 = \tilde{Q}_{2,0}e^{-j\omega t}$ , which leads to the following linear system.

$$\begin{bmatrix} A11 & A12 \\ A21 & A22 \end{bmatrix} \begin{Bmatrix} \tilde{Q}_{1,0} \\ \tilde{Q}_{2,0} \end{Bmatrix} = 0 \quad (14)$$

By setting the determinant of the matrix  $A$  to zero we obtain the system characteristic equation that is a third order equation in terms of  $j\omega$ .

$$\begin{vmatrix} A11 & A12 \\ A21 & A22 \end{vmatrix} = A11A22 - A12A21 = a(j\omega)^3 + b(j\omega)^2 + cj\omega + d = 0 \quad (15)$$

The solutions for this equation are the system poles, in form of  $j\omega = \omega_R + j\omega_I$ . Where  $\omega_I$  is the system natural frequency and  $\omega_R$  the system damping. Instability is reached when the system damping is negative.

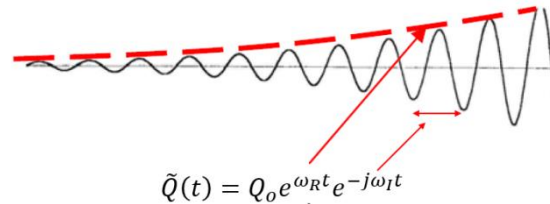


Figure 14 – Negative damping (Fleming et. al, 2009)

#### 4.1 Parameters computation via CFD

Computational numerical simulations CFD were performed in order to compute the following parameters: Draft tube loss coefficient ( $\zeta_2$ ), Mass flow gain factor ( $\chi$ ), Cavitation compliance ( $C$ ) a Vortex pressure coefficient ( $\alpha$ ).

Mean mass flow rate at spiral case inlet ( $\rho Q$ ) and static pressure ( $\rho gH$ ) at draft tube extended zone outlet were set as boundary conditions. Nonslip wall option was chosen for all domains walls.

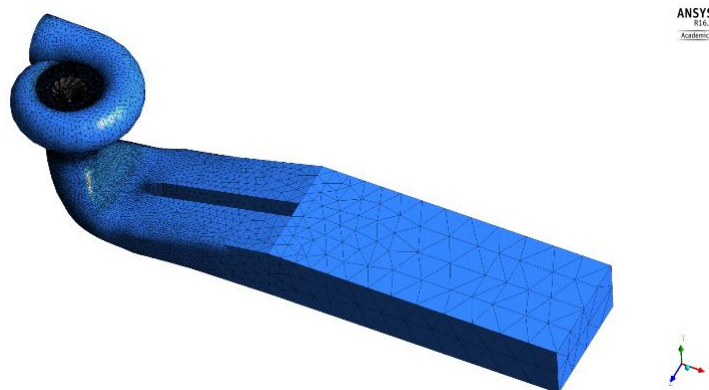


Figure 15 – Complete CFD domain

The computational mesh is an unstructured tetrahedral dominant mesh. Table 7 shows the number of elements for each mesh domain and its minimum orthogonal quality. Grid convergence tests for same meshing approach were carried out in the work produced by Marra et. al (2015).

**Table 7 – Mesh figures**

Domain	No Elements	Minimum Orthogonal Quality
Draft Tube	6.375.068	0.12
Spiral Case	3.344.910	0.12
Runner	7.057.670	0.18
Total	16.777.648	0.12

Computational resource used was 10 cores of an Intel ® Xeon ® E5-1650 CPU of 3.2 GHz processor, 16GB of RAM in a 64-bit windows 7 operating system.

Steady state monophasic simulations were run in accordance with Flemming et. al (2009). Simulations were carried out in two computations stages. Firstly, a steady state computation configured with SST turbulence model and upwind advection scheme was performed. The previous result was used to initialize the final computation where advection scheme was changed to High Resolution. A RMS residual of 1E-4 was set as convergence criteria and the mean computational time spent was 4.5 hours for each computation.

A numerical simulation (SIM1), following the aforementioned procedure, was performed for the operating point when the unit generates 740MW with 96% of wicket gate opening. The boundaries conditions are shown in Table 8, where  $Q$  is the mean discharge at spiral case inlet and  $H$  is the static head at draft tube outlet, or counter-pressure.

**Table 8 – Boundary conditions**

Simulation	$Q[m^3/s]$	$H [m]$
SIM1	703	29
SIM2	703	32
SIM3	738	29

Two additional simulations, SIM2 and SIM3, around the nominal operating point (SIM1) were performed with 10% of variation in the outlet head ( $H$ ) and 5% in de discharge ( $Q$ ) respectively, as seen in Table 8.

From the definition of the parameters  $\chi$  e  $C$  presented in Eq. (7), a discrete version given by a forward finite difference is shown in equations (16) and (17).

$$C = -\frac{1}{\rho g} \left( \frac{V_{SIM2} - V_{SIM1}}{H_{SIM2} - H_{SIM1}} \right) \tag{16}$$

$$\chi = -\left( \frac{V_{SIM3} - V_{SIM1}}{Q_{SIM3} - Q_{SIM1}} \right) \tag{17}$$

By applying the vortex volume found in CFD simulations, as in Figure 16, and the boundary conditions presented in Table 8 we can obtain the values presented in Table 9.

**Table 9 – Vortex parameters**

Simulation	Volume [m <sup>3</sup> ]	$\chi$ [s]	$C$ [m <sup>4</sup> s <sup>2</sup> /kg]
SIM1	2,26		
SIM2	1,78	$-5.34 \times 10^{-2}$	$1.64 \times 10^{-5}$
SIM3	4,13		

The vortex volume was set to be all volume fraction below vapor pressure at 25°C ( $P_c = P_v = 3.17$  kPa).

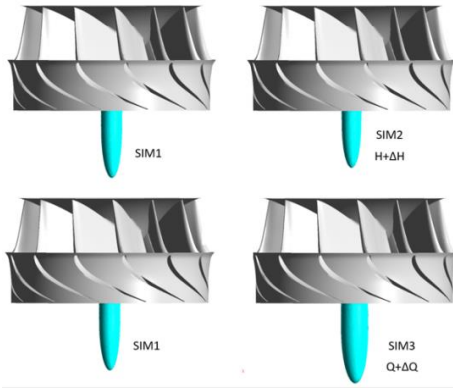


**Figure 16 – Vortex volume found in simulations**

One alternative method to find the Cavitation Compliance ( $C$ ), similar to the one adopted by Alligné et al. (2010), consist in an interactive change in  $C$  until the natural frequency given by the mathematical model match the frequency measured in field test on prototype. Result for this approach is found in Table 10.

**Table 10 – Alternative Cavitation Compliance**

Frequency of the Oscillation Prototype [Hz]	Cavitation Compliance $C_2$ Estimated [m <sup>4</sup> s <sup>2</sup> /kg]
0.85	$7.25 \times 10^{-5}$

The computation of  $\zeta_2$  is performed based on equations (18) and (19), and mean total pressure at Draft tube inlet (CFD simulation 1), as shown in Figure 17 (a).

$$\zeta_2 = f \frac{L}{D} + K \tag{18}$$

$$K = \frac{2(P_{1o} - P_{2o})}{\rho \bar{V}^2} \tag{19}$$

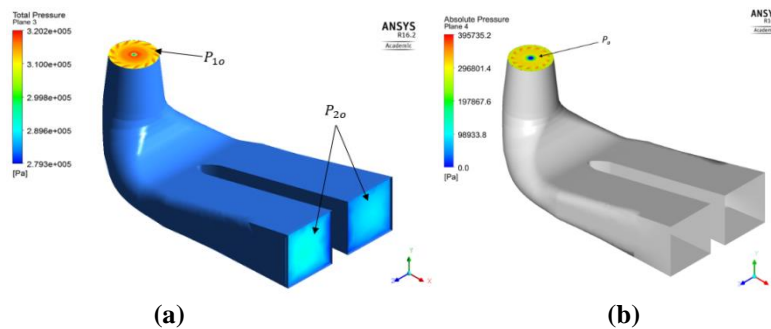


**Figure 17 – (a) Mean total pressure plane (CFD – SIM1);(b) Mean static pressure plane (CFD-SIM1).**

Vortex pressure coefficient  $\alpha$  is evaluated by Eq.(20) and mean static pressure measured in CFD simulation (SIM1) at Draft tube inlet, as in Figure 17 (b).

$$\alpha = \frac{p_a - p_c}{\rho C_\theta^2} \quad (20)$$

## 4.2 Case study

Pressure pulsations, in the interval between  $t = 2.8$  s and  $t = 8.6$  s in Figure 18, indicate a limit stability operation.

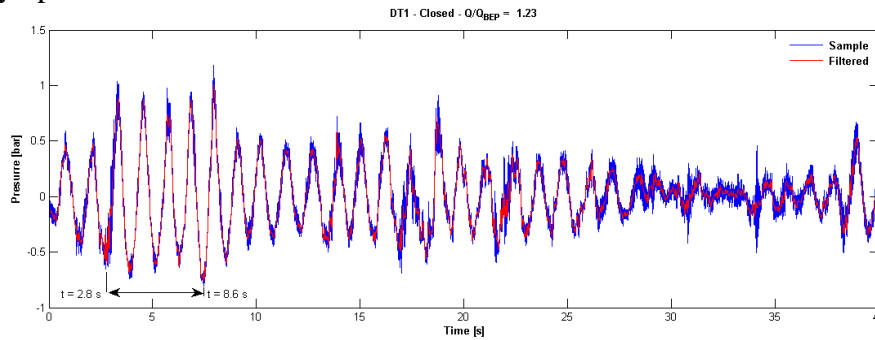


Figure 18 - Possible stability limit prototype operation

This condition is reached when the prototype is generating 740 MW of active power, for 96% of wicket gate opening,  $Q/Q_{BEP} = 1.23$  (full load), net head of 116m and without aeration. After windowing that interval, frequency response analysis shows an pressure oscillation of 6% zero-peak of the prototype specific energy at 0.85 Hz ( $f/f_n = 0.57$ ).

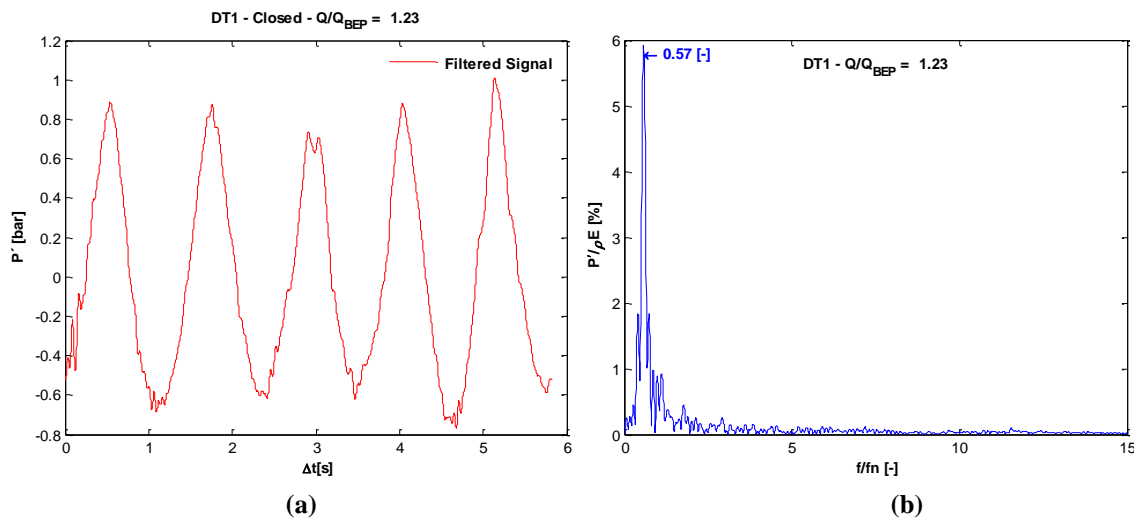


Figure 19 – Filtered windowed pressure signal (DT1) – (a) Time domain; (b) Frequency domain

Hence, the criteria given by equation (21), suggested by Dörfler et. al (2013), is not satisfied ( $13.5 > 10.7$ ), which characterize this pressure pulsation as abnormal.

$$\Delta h_{p-p} < \sqrt{H} \quad (21)$$

The dynamical one dimensional model for full load stability analysis, presented in section 4 , is applied resulting in the stability diagram of Figure 20 (a), which shows stable and unstable zones as function of the hydroacoustic parameters  $\chi$  and  $C$ .

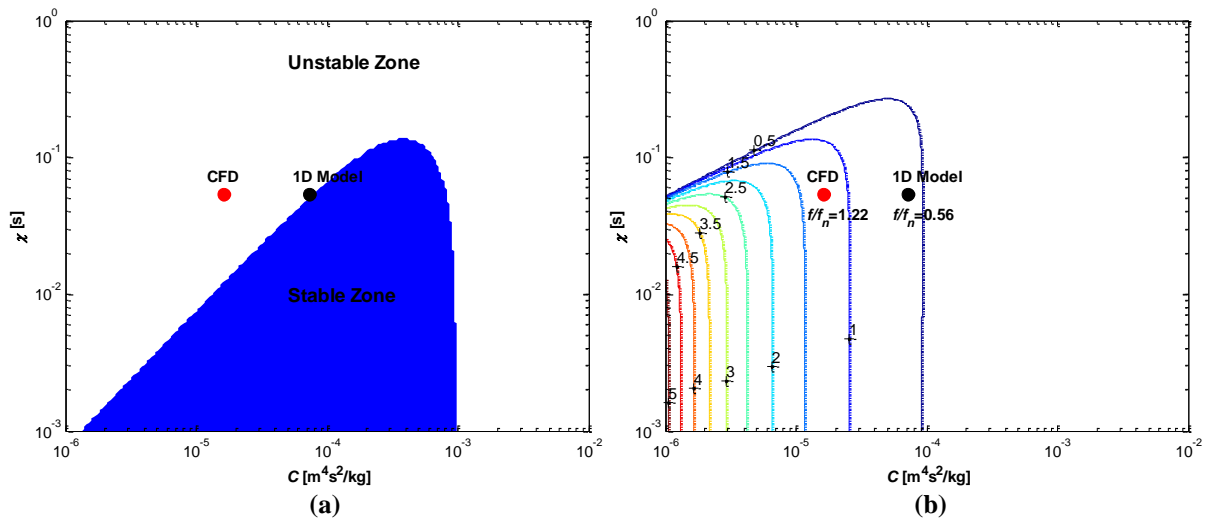


Figure 20 – (a) Stability Diagram; (b) System natural frequencies – ITAIPU’s Prototype

As observed in Figure 20 (a), both methods for the evaluation of Cavitation Compliance (C) predicted instability. The approach that used the 1D model and field measurements to evaluate C predicted limit stability operation (transition stable-unstable) whereas the approach that used only CFD predicted a complete unstable operation. The destabilizing effect of the  $\chi$  is verified, once the more it increases, for fix value of C, farther the system goes from a stable condition, as seen in the diagram.

Aeration effect can be verified based in field test results that show a reduction of 18% (from 0.56 Hz to 0.46 Hz, as seen in Table 5) in oscillation frequency. This way, a new Compliance C for the system is computed by equation (22), which results in a value 48% higher than the original one.

$$C_2 = \left(\frac{f_1}{f_2}\right)^2 C_1 \quad (22)$$

As a result, the operation points shifted towards a stable zone, as seen in Figure 21 (a).

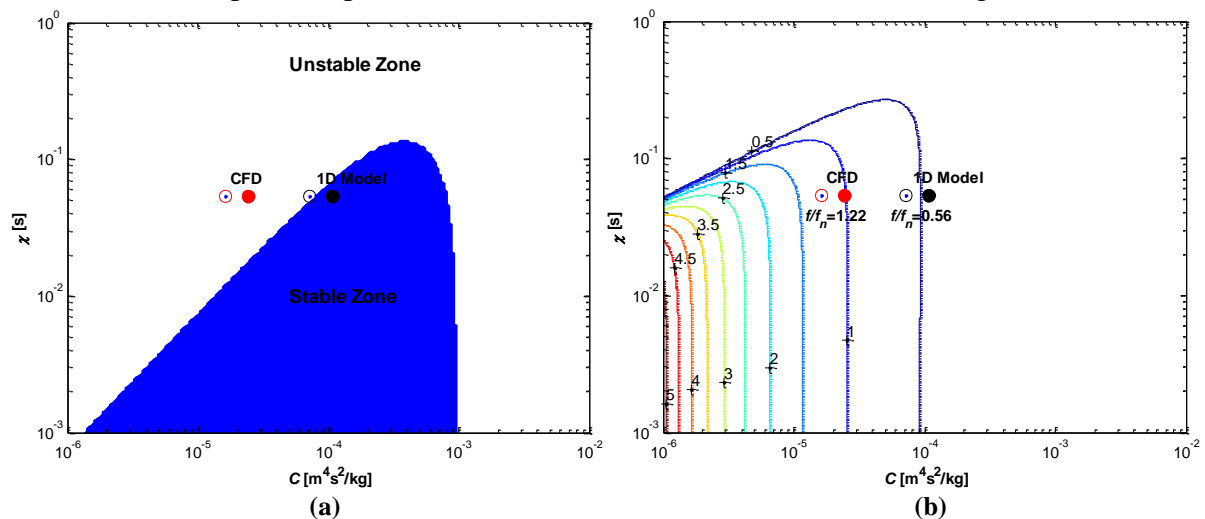


Figure 21 – Aeration effect – (a) Stability diagram; (b) System natural frequencies

This result is corroborated by the field tests performed for this operating condition, which shows a stabilizing effect of the aeration.

## 5 CONCLUSIONS

Regarding to aeration effectiveness on the prototype, it is evident its good performance in full load conditions. This was an expected fact, given the reason that this device was installed in ITAIPU turbines. In contrast, for part load conditions, based on field tests, the aeration effect was not relevant from the point of view of change of the system dynamical response. From the quantitative point of view, measurements of the mean airflow rate through the aeration duct shows that an air flow of 1.3% of the turbine rated discharge is sufficient to reach the higher potential attenuation of the pressure pulsations for a specific operating point where the pressure reduction was up to 90%.

Both Cavitation Compliance modeling methods were able to predict instability for this case study. In addition, the aeration effect was inserted in an indirect way into the model, which responded in accordance with the field tests.

Even though this methodology to model full load instability has shown satisfactory results and good potential to evaluate hydraulic instability, it cannot be stated that the model is validated, once more operating conditions need to be simulated, given the simplifications of the model and the inherent imprecision to predict complex hydroacoustic parameters by means of monophasic CFD computations.

## ACKNOWLEDGMENTS

The authors would like to express their sincere gratitude to the staff of the Test Sector of the Laboratory Division - SMIL.DT, the Mechanical Maintenance Division - SMMU.DT of ITAIPU BINACIONAL and the support of the Center for Advanced Studies on Safety of Dams – CEASB belonging to the Itaipu Technological Park – PTI which especially we thank for the availability of the necessities computing resources for this work.

## REFERENCES

- Alligné, S., 2011. *Forced and Self-Oscillations of Hydraulic Systems Induced by Cavitation Vortex Rope of Francis Turbines*. Lausanne: École Polytechnique Fédérale de Lausanne.
- Alligné, S. et al., 2010. Prediction of a Francis Turbine Full Load Instability From Investigations on the Reduced Scale Model. *25th IAHR Symposium on Hydraulic Machinery and Systems*. Timisoara.
- Chen, C. et al., 2008. One-Dimensional Analysis of Full Load Draft Tube Surge. *Journal of Fluids Engineering*, Vol. 130.
- Dörfler, P., Sick, M. & Coutu, A., 2013. *Flow-Induced Pulsation and Vibration in Hydroelectric Machinery*. s.l.: Springer London.
- Flemming, F., Foust, J., Koutinik, J. & Fisher, R., 2009. Overload Surge Investigation Using CFD Data. *International Journal of Fluid Machinery and Systems*, Vol. 2.
- Landry, C., 2015. *Hydroacoustic Modeling of a Cavitation Vortex Rope for a Francis Turbine*. Lausanne: École Polytechnique Fédérale de Lausanne.

Lipej, A. et al., 2009. Numerical Prediction of Pressure Pulsation for Different Operating Regimes of Francis Turbine Draft Tubes. *International Journal of Fluid Machinery and Systems*, Vol. 4.

ITAIPU, 2015. *Estudo para Avaliação da Influência da Aeração no Comportamento Hidráulico das Turbinas*. Technical Report. Itaipu Binacional. Foz do Iguassus.

Marra, J. M., Gramani, L. M., Zubeldia, L. F. & Kaviski, E., 2015. Turbulence Models Comparison in a Francis Turbine Flow Simulation: An Applied Case on the Itaipu Turbines. *Proceedings of the XXXVI Iberian Latin-American Congress on Computational Methods in Engineering*. Rio de Janeiro.

Müller, A., 2014. *Physical Mechanisms governing Self-Excited Pressure Oscillations in Francis Turbines*. Lausanne: École Polytechnique Fédérale de Lausanne.

Nicolet, C., 2007. *Hydroacoustic Modelling and Numerical Simulation of Unsteady Operation of Hydroelectric Systems*. Lausanne: École Polytechnique Fédérale de Lausanne.

Pejovic, S., 2002. Troubleshooting of Turbine Vortex Core Resonance and Air Introduction Into Draft Tube. *XXI IAHR Symposium on Hydraulic Machinery and Systems*. Lausanne.

Pejovic, S., Obradovic, D. & Gajic, A., 1986. Field Tests and Calculations of Effects of Air Introduction Into the Draft Tube upon Hydraulic Oscillations in a Hydropower Plant. *IAHR Symposium*. Montreal.

Qian, Z.-d., Yang, J.-d. & Huai, W.-x., 2006. Numerical simulation and analysis of pressure pulsation in francis turbine with air admission. *Journal of Hydrodynamics*, August.